# 2

# Optical Nonlinearity in Metal Nanoparticles

## 2.1 Metal nanoparticles

The term 'cluster' is defined as an entity consisting of 3 to $10^7$ atoms of uniform or mixed chemical composition, packed densely with arbitrary external shape and structural arrangement. '*Metal clusters*' are composed of materials which in the bulk state are classified as metals with a high density of electronic states near the Fermi level. In the state of clusters, they may not exhibit metallic properties [Kreibig]. Clusters are intermediate between atoms on one side and solid or liquid on the other, with widely varying material properties. Metal clusters that are large enough to posses a well defined conduction band, and hence, are able to manifest plasmon resonance and classical electron charging behaviour, are termed as *'metal nanoparticles'* [Feldheim, D. L.]. The number of atoms situated at the surface of a cluster can be more than the number of atoms inside the cluster, thus giving rise to interesting new properties from the interaction of the large fraction of the surface atoms with the surrounding medium. If the diameter of the cluster is in the 1-3 nm range, it is named as a '*small*' cluster. The ratio of the number of atoms on the surface of the cluster to that in the interior of the cluster will be between 50% and 90% for small clusters. If the cluster diameter is in the 3 –100 nm range, it is categorized as a '*large*' cluster. The surface to volume ratio is ≤ 50% in this case. Clusters having a size ≤1nm are named as *'very small'* clusters. Here the surface and the inner volume are not separable, or in other words, most of the atoms will be at the surface. Very small clusters are regarded as *molecule-lik*e structures whereas the large clusters are considered as *tiny, size-limited solids*. Electrical and optical properties of clusters strongly depend on their size, shape and the surrounding medium. Usually the clusters in matrices or in

supports will be large clusters [like the core-shell nanoparticles and doped polymer films of our studies]. Small and large clusters are usually approximated as spheres and spheroids respectively, if they are in free form. If they are embedded or supported they are categorized as ellipsoids and caps respectively [Kreibig]. The optical properties of metal nano clusters are interesting in different size ranges. There are two different kinds of cluster size effects: *intrinsic effects* - concerning specific changes in volume and surface material properties - and *extrinsic effects* – which are size-dependent responses to external fields or forces irrespective of the intrinsic effects. For large clusters electrodynamic theory can be applied using bulk optical constants (extrinsic size effects). For small sized clusters, the optical functions become size-dependent (intrinsic size effects). The dielectric functions of clusters with diameter larger than 10nm are usually close to those of the bulk material and are size independent.

### 2.1.1 Surface plasmon resonance

The noble metals silver (Ag) and gold (Au) have completely filled 4d and 5d bands and just one electron in the 5s and 6s bands respectively. Atomic number of bulk Ag is 47 with the outermost orbital configuration given as $4d^{10}$, $5s^{1}$; and for Au it is 79 with the configuration $4f^{14}$, $5d^{10}$, $6s^{1}$. When these metals form nanoclusters distinct energy bands are formed unlike in the case of bulk metals. At a fundamental level, the linear absorption spectra reveal the electronic structure of metal nanoclusters. The linear absorption spectra of metallic nanoclusters exhibit a strong broadband absorption, which is absent in the spectra of the bulk metals. For small nanoclusters this will be a nearly featureless curve that stretches from the near infrared to the near ultraviolet, which corresponds to interband transitions from the d band to the sp band. For Au nanoclusters the interband transitions occur between the $5d^{10}$ band and the unoccupied states of the conduction (6sp) band. The transition starts near 1.6eV, which is the energy difference between the highest occupied state of the d-band and the lowest unoccupied state of the conduction band. There are also intraband transitions occurring within the broad conduction band (derived mainly from the $6s^{1}$p hybridized atomic orbitals of Au)

that start at zero frequency. These intraband transitions in the conduction band are common to all metals. It depends on the square of the input frequency till it approaches the surface plasmon frequency where resonant absorption takes place.

Metals have a large number of conduction electrons, which form a free electron gas. The negative charge of the conduction electrons is balanced by an equal number of positive charges of the ion cores. A collective excitation of the conduction electrons in a metal is known as '*plasma oscillation'*. The frequency of this plasma oscillation is given by $\omega_p = \sqrt{\frac{ne^2}{m\varepsilon_0}}$ where *n* is the free electron density, *e* the charge of the electron, *m* its mass and $\varepsilon_0$ the permittivity of free space. This is known as the *plasma frequency* of a metal. *'Plasmons*' are the quanta of this plasma oscillation, similar to photons being the quanta of electro-magnetic fields. For bulk metals the plasma frequency is called '*volume plasmon frequency'*. In most metals the volume plasmon frequency is in the ultraviolet so that visible light reflects from them, making them shiny. For a metal like copper the volume plasmon frequency is in the visible whereas for gold it is in the deep ultraviolet. The volume plasmon energy is estimated as:

$$E_p = \hbar\omega_p \tag{2.1}$$

Those plasmons that are confined to the surface and interact strongly with light resulting in a polariton are known as '*surface plasmons*'. They occur at the interface of two materials with different dielectric constants.

When excited with light, the conduction electrons in a bulk metal behave as a relaxator system. When the metal is in the form of spherical clusters they behave like an oscillator system, with polarization charges at the cluster surface giving rise to a linear restoring force that determines the energy eigen frequencies of the system. These are interpreted as classical *surface plasmon frequencies*. Although all the electrons oscillate in the positive ion background, the main effect

producing the restoring force is the surface polarization [Kreibig pg.24]. The resonant position of the multipolar surface plasmon polariton eigen frequencies is given by the expression (in the quasi-static limit of Mie theory applied to electrically neutral clusters)

$$\omega_L = \omega_p \frac{1}{\sqrt{1+\frac{L+1}{L}\varepsilon_m}} \tag{2.2}$$

where L is the order of the multipole.

For spherical metal clusters with the cluster radius << wavelength of the interacting electromagnetic field, the extinction cross section is given by Mie theory as

$$\sigma_{ext}(\omega) = 9\frac{\omega}{c}\varepsilon_m^{3/2}V_0\frac{\varepsilon_2(\omega)}{\left|\varepsilon_1(\omega)+2\varepsilon_m\right|^2+\varepsilon_2{}^2(\omega)} \tag{2.3}$$

where the phase retardation and effects of higher multipoles are neglected. Here $V_0$ is the particle volume, $\varepsilon_m$ is the dielectric function of the embedding medium that is assumed to be frequency-independent over the spectral range of interest, and $\varepsilon_1(\omega)$ and $\varepsilon_2(\omega)$ are the real and imaginary parts of the dielectric constant of the spherical metal cluster. Since only the dipolar absorption is considered, [Kreibig pg.31] the expression gives the absorption cross section of the dipolar surface plasmon. The absorption peak occurs when $\left|\varepsilon_1(\omega)+2\varepsilon_m\right|^2+\varepsilon_2{}^2(\omega)$ is a minimum. $\varepsilon_1(\omega)$ determines the peak position and also influences the width of the resonant absorption. Steep $\varepsilon_1(\omega)$ spectra give sharp resonances whereas slowly varying $\varepsilon_1(\omega)$ gives broad absorption bands. Small $\frac{d\varepsilon_1(\omega)}{d\omega}$ and large $\varepsilon_2(\omega)$ smear out the resonances. Noble metals are found to exhibit sharp resonances [Kreibig pg.33]: for instance Ag shows a pronounced surface plasmon resonance in vacuum due to small $\varepsilon_2(\omega)$ at 3.6eV. By embedding the metal nanoclusters in transparent dielectric materials their surface plasmon resonance frequencies can be tuned, as the plasmon resonance positions depend on the refractive index of the surrounding material. This is termed *immersion spectroscopy*. This will give a

surface plasmon resonance to Au, which is normally absent in vacuum. However, this broad surface plasmon resonant absorption in Au nanoclusters starts diminishing as the nanocluster size decreases from approx. 10nm towards a core size of 1nm, where the linear absorption spectrum becomes a nearly featureless curve that represents only interband and intraband transitions. The high polarizability of the $5d^{10}$ core largely red shifts the collective-resonance in the Au nanoclusters to the observed location of 2.4eV. Thus the absorption peak at 2.4eV of Au nanoclusters is originated by the intraband transition and modified by the polarizability of the $5d^{10}$core [Alvarez, M. M.].

## 2.2 Physics of nonlinear light transmission

Depending on the characteristic response of the medium to the frequency of light, the transmission of light through a medium gets affected by the scattering or absorption of light by the medium. When the intensity of the input light is such that the corresponding electric field is sufficient to evoke the otherwise small nonlinear terms in the dipole oscillation, it modifies the properties of the medium. The light will in turn get affected. The change in transmittance of a medium as a function of the input intensity or fluence is referred to as nonlinear absorption or nonlinear light transmission. At sufficiently high intensities, the probability of an absorber absorbing more than one photon before relaxing to the ground state can be enhanced.

### 2.2.1 Two-photon absorption

The process of the transition of a system from the ground state to a higher level by the simultaneous absorption of two photons from an incident radiation field is known as two-photon absorption. Two-Photon Absorption (TPA) spectroscopy complements linear absorption spectroscopy in studying the excited state of a system. Here two photons of frequency $\omega$ from the incident field are simultaneously absorbed by the system to make the transition to a state that is

approximately or exactly resonant at 2ω. The intermediate level being virtual, the two photons should be simultaneously absorbed making the process sensitive to the instantaneous optical intensity of the incident radiation. On the other hand, the two-step absorption that involves a single photon pumped real intermediate state is referred to as *excited state absorption*. The two-photon absorption process is proportional to the square of the input intensity. The propagation of the laser light (which is sufficiently intense to initiate the nonlinear light –matter interaction), through the system describing the optical loss is given by

$$\frac{dI}{dz} = -\alpha I - \beta I^2 \tag{2.4}$$

where α is the linear absorption coefficient (which can be very small) and β the two-photon absorption coefficient. β is a macroscopic parameter that characterizes the material and is related to the individual molecular TPA absorption cross section $\sigma_2$ through

$$\sigma_2 = \frac{\hbar\omega\beta}{N} \tag{2.5}$$

where N is the number density of the molecules in the system and ω is the incident radiation frequency. It is the imaginary part of the third order nonlinear susceptibility of the system that determines the strength of two-photon absorption. The relation between the TPA coefficient and the third order susceptibility of a centrosymmetric system for linearly polarized incident light is given as:

$$\beta = \frac{3\pi}{\varepsilon_0 n^2 c\lambda}\,\mathrm{Im}[\chi^{(3)}_{xxxx}(-\omega;\omega,\omega,-\omega)] \qquad \text{(in SI units)} \tag{2.6}$$

Since the physical quantity that is measured is the transmitted energy in a typical light transmission measurement, the transmittance is conveniently defined as the ratio of the transmitted and incident energies. For a pulsed laser beam that is spatially and temporally Gaussian the transmittance T in the presence of TPA is given as: [Sutherland]

$$T = \frac{(1-R)^2 \exp(-\alpha L)}{\sqrt{\pi} q_0} \int_{-\infty}^{\infty} \ln[1 + q_0 \exp(-\tau^2)]\, d\tau \tag{2.7}$$

where R is the Fresnel reflection at the interface of the material with air, $\alpha$ the linear absorption coefficient and L the length of the medium. $q_0$ is given by

$$q_0 = \beta(1-R)I_0 L_{eff} \tag{2.8}$$

where $I_0$ is the peak on-axis intensity incident on the material from air. The effective length in the medium is given as

$$L_{eff} = \frac{1-\exp(-\alpha L)}{\alpha} \tag{2.9}$$

### 2.2.2 Three-photon absorption

The simultaneous absorption of three photons by a system from an incident radiation field is known as three-photon absorption (3PA). It is a fifth order nonlinear process, and the propagation equation for a medium having significant three-photon absorption is given by

$$\frac{dI}{dz} = -\alpha I - \gamma I^3 \tag{2.10}$$

where $\alpha$ is the linear absorption , which can be typically small, and $\gamma$ is the three-photon absorption coefficient. For a centrosymmetric system and linearly polarized light, $\gamma$ is related to the imaginary part of the fifth order susceptibility through [Sutherland pg. 589]

$$\gamma = \frac{5\pi}{\varepsilon_0{}^2 n^3 c^2 \lambda} \mathrm{Im}[\chi^{(5)}_{xxxxxx}(-\omega;\omega,\omega,\omega,-\omega,-\omega)] \text{ (in SI units)} \tag{2.11}$$

The transmittance of a system with three-photon absorption, when the incident laser is spatially and temporally Gaussian, is given as:

$$T = \frac{(1-R)^2 \exp(-\alpha L)}{\sqrt{\pi} p_0} \int_{-\infty}^{\infty} \ln[\sqrt{1+ p_0{}^2 \exp(-2\tau^2)} + p_0 \exp(-\tau^2)] d\tau \tag{2.12}$$

where $p_0 = \sqrt{2\gamma(1-R)^2 I_0{}^2 L_{eff}^{'}}$ (2.13)

with $L_{eff}^{'} = \frac{1-\exp(-2\alpha L)}{2\alpha}$ (2.14)

### 2.3 The open aperture z-scan setup

We used the open aperture zscan experiment [Sheik Bahae *et al.*] to measure the nonlinear transmission in the samples. The experimental set up is given in figure 2.1. Liquid samples were taken in a 1 mm quartz cuvette.

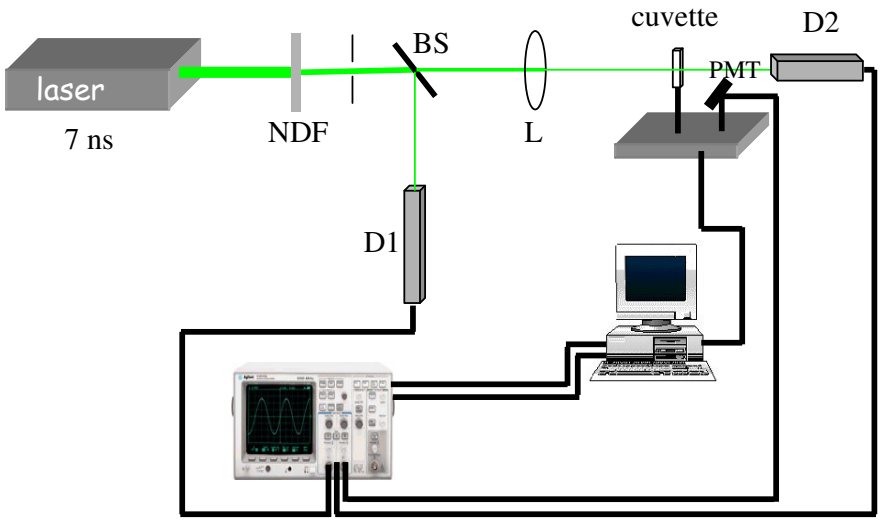


Figure 2.1: The open aperture zscan experimental set up. NDF: Neutral density filters, BS: Beam Spliter, L: Lens, D1 & D2: Detectors 1 & 2.

In the z-scan, the laser beam is focused using a lens, and the sample is translated along the beam axis (z-axis) through the focal region, over a length several times that of the confocal distance. The focal point is taken as z=0. At each position z the sample sees a different laser fluence, and the position dependent (i.e., fluence dependent) transmission T(z) is measured using a pyroelectric energy probe placed after the sample. The graph plotted between z

and T (z) is known as the open aperture z-scan curve. The focal beam spot size is measured to be 20 ± 2 μm in our experiment. By running the laser flash lamps at full power, the pulse to pulse energy stability is improved to better than ±5%; these small fluctuations are nevertheless accounted for by using a reference energy probe in the experiment. Energy reaching the sample is appropriately reduced using neutral density filters. The samples are subjected to a smoothly varying input laser intensity by scanning them through the focal region by using a stepper motor driven translation stage. Data acquisition is done using a storage oscilloscope that is interfaced to a computer via serial port communication. The stepper motor also is controlled by the computer using the parallel port. By fitting the z-scan curve to eqn. 2.7 (for two-photon/two step process) or 2.12 (for three-photon process), the nonlinear absorption coefficient is calculated.

### 2.4 Oxide-protected Au and Ag core-shell nanoparticles

Core–shell metal nanoparticles have a well-defined core as well as a shell, both in the nanometer size range. These are synthesized by encapsulating the nanometal core within a shell of desired material or by coating the nanometal core by suitable shell material [Danek *et al.*], [Dabbousi *et al.*]. Depending on the nature of the core and the shell materials, the core-shell nanoparticles investigated in the present studies can be subcategorized as metal-metal oxide and bimetallic - metal oxide types [Pradeep, T.], [Zhong *et al.*]. These samples were synthesized by the group of Prof. T. Pradeep at the Indian Institute of Technology Madras, Chennai.

The nanoparticle samples Au@$TiO_2$, Au@$ZrO_2$, Au@$SiO_2$ and Ag@$ZrO_2$ in the size range of 30–60 nm, of which the nonlinear light transmission properties are studied here, belong to the metal-metal oxide core-shell group of metal nanoparticles. Oxide protection is one way to make metal nanoparticles stable under extreme conditions. Even after irradiating the present oxide-protected nanoparticles with laser pulses of fluences up to 20 $Jcm^{-2}$ and intensities up to

2.8 GW $cm^{-2}$, no signs of damage were observed. In addition to the stability offered against high irradiation and particle coalescence, the inorganic coating of the metal nanoparticles also changes their optical properties.

In this section, we discuss features of nonlinear optical transmission observed in the clusters $Ag@ZrO_2$, $Au@SiO_2$, $Au@ZrO_2$ and $Au@TiO_2$ suspended in 2-propanol, when excited with nanosecond laser pulses at 532 nm. Results show that the samples have a high laser damage threshold and can be used either as saturable absorbers or optical limiters in the appropriate laser fluence regimes. Fig.2.2A shows the absorption spectra of the nanoparticles. For $Ag@ZrO_2$ the plasmon absorption maximum is at 421 nm. The redshift of the peak from 400 nm (absorption maximum of bare nanoparticles) is due to the dielectric shell surrounding the metal core [Tom *et al.*]. The plasmon absorption maxima of $Au@ZrO_2$ and $Au@SiO_2$ are at 527 and 533 nm, respectively. The absorption peak shifts are dependent on the shell thickness [Ung *et al.*], [Tom *et al.*]. The transmission electron micrograph (TEM) of $Ag@ZrO_2$ given in Fig. 2.2B is an expanded image of a single nano particle with Ag core and $ZrO_2$ shell, depicting a typical particle size of 50 nm and a shell thickness of 3 nm. It must be noted that the shell covers the core completely. For $Au@SiO_2$ the Au core is of 10–15 nm diameter while the shell is of about 4-nm thickness. TEM did not reveal the presence of free particles of metals or oxides.

To investigate the transmission properties of the nanoparticles, we used 7 ns (FWHM) pulses from a Q-switched Nd:YAG laser emitting at the second harmonic wavelength of 532 nm (2.33 eV). From actual beam profile measurements using the knife-edge method, the spatial intensity profile of the laser is confirmed to be near Gaussian. The intensity dependent transmission is measured using the automated open aperture z-scan set-up discussed above.

Since the nonlinear behavior exhibited by the samples was found to be somewhat similar, only $Au@SiO_2$ and $Ag@ZrO_2$ were studied in greater detail as

representative samples. Figs. 2.3a and 2.3b show the z-scan curves obtained for $Au@SiO_2$ suspended in 2-propanol at various concentrations, for laser energies of 15 and 39 μJ, respectively. Figs. 2.3c and 2.3d depict the corresponding results obtained in the $Ag@ZrO_2$ samples. The z-scans obtained are peculiar in that an increase in transmission is seen at moderate laser fluences, while the transmission drastically decreases at higher fluences. The increase in transmission is more pronounced at higher concentrations as seen from Fig. 2.4, in which the z-scans

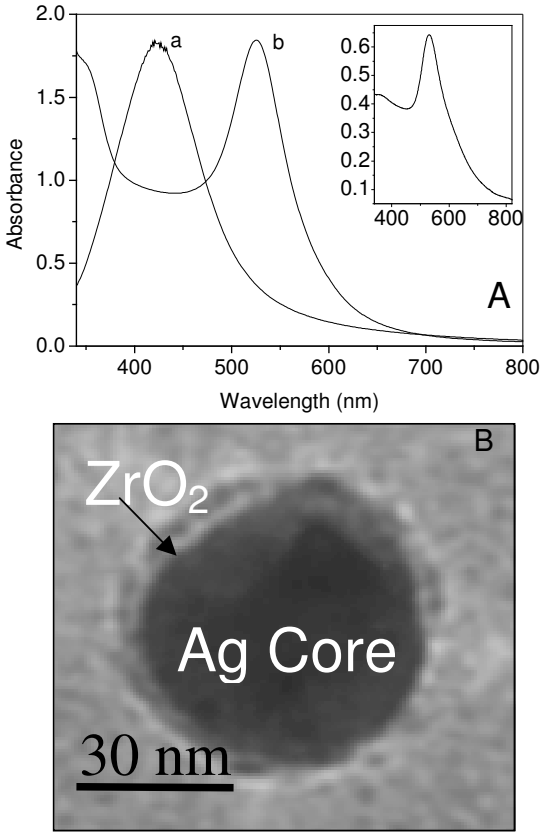


Figure 2.2: (A) The optical absorption spectrum of $Ag@ZrO_2$ (a), $Au@ZrO_2$ (b) and $Au@SiO_2$ (inset) nanoparticle suspensions. The absorption spectrum peaks at 421 nm for $Ag@ZrO_2$. For $Au@ZrO_2$ and $Au@SiO_2$, the peak maxima are at 527 and 533 nm, respectively, for a 3 nm shell thickness. (B) The transmission electron micrograph of $Ag@ZrO_2$. A $ZrO_2$ shell of about 3-nm thickness is seen in the TEM.

obtained for two concentrated suspensions of $Ag@ZrO_2$ for 5μJ pumping are shown. The normalized transmittance as a function of the incident laser fluence is shown in Fig. 2.5, for all samples. The samples have been irradiated up to a fluence of 20 J $cm^{-2}$ without any signs of laser-induced damage.

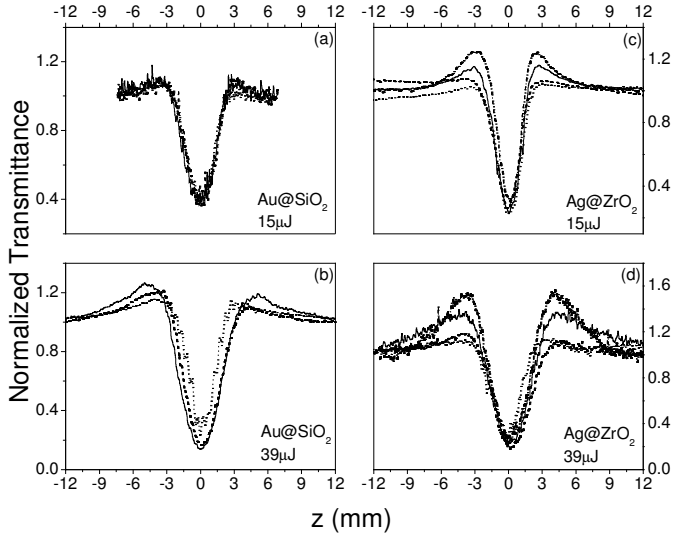


Figure 2.3: The z-scan curves obtained for $Au@SiO_2$ and $Ag@ZrO_2$ suspensions. Laser pulse energies of 15 and 39 μJ are used. Sample linear transmissions at 532 nm are: dash-dotted line – 0.38, solid line – 0.48, dashed line – 0.58, and dotted line – 0.68.

To explain these results, it may be noted that for noble metals, in particular gold, the optical properties are determined by the 5d and 6sp (conduction) band electrons. The outermost d and s electrons of the constituent atoms together form a total of six bands, with five of them (the d bands) fairly flat and lying a few eV below the Fermi level, while the sixth band (the sp band) is almost free electron-like: roughly parabolic with an effective mass very close to that of an electron. The observed increase in transmission at moderate laser fluences can be explained on the basis of surface Plasmons. A singular property of the SPR is that it leads to a large local field enhancement within the metal particle. This effect can be appreciable with laser excitation, where the electric field associated with the

electromagnetic radiation is quite high. In the quasi-static limit the local field inside a spherical particle $E_{loc}$, is related to the applied field $E_0$

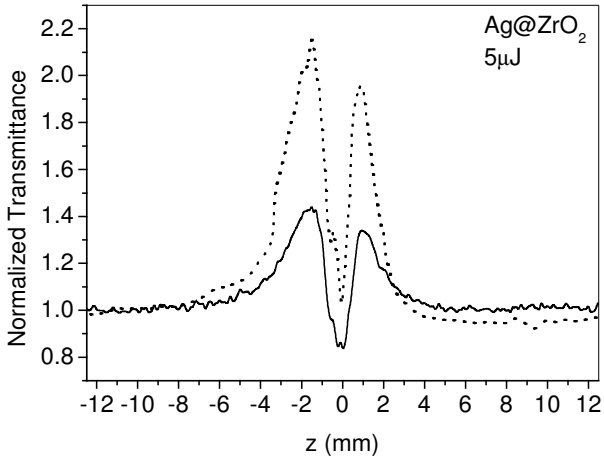


Figure 2.4: The z-scans obtained for concentrated suspensions of $Ag@ZrO_2$ . Linear transmission is 0.2 for the dotted line and 0.3 for the solid line. Laser pulse energy is kept low at 5 μJ.

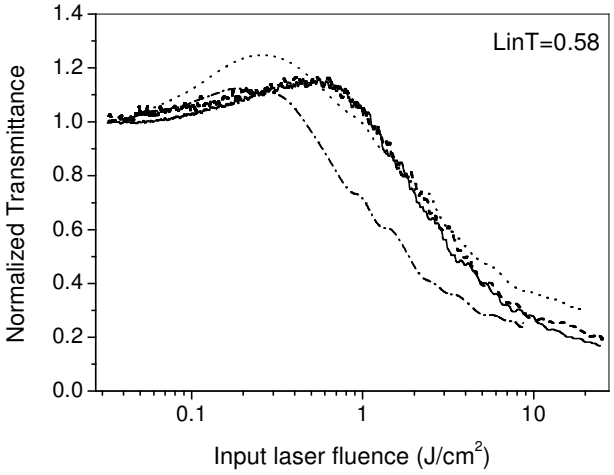


Figure 2.5: Normalized transmittance of the suspensions, as a function of the input laser fluence. Linear transmission is 0.58 for all samples. Dashed line – $Ag@ZrO_2$, solid line – $Au@SiO_2$, dotted line – $Au@TiO_2$, and dash-dotted line – $Au@ZrO_2$.

by $E_{loc} = [3\varepsilon_m(\omega)/(\varepsilon_m(\omega) + 2\varepsilon_d(\omega))]E_0 = f(\omega)E_0$, where $\varepsilon_d$ is the dielectric constant of the surrounding medium; $f(\omega)$ is defined as the local field factor. At the SPR peak the local field factor has the maximum value, given by $|f_{max}(\omega p)|^2 = |3\varepsilon_1/2\varepsilon_2|^2$. Since the real part of the dielectric constant is larger than the imaginary part in noble metals, they experience strong local field enhancements upon laser irradiation. Therefore, the effective third order nonlinear susceptibility $\chi^{(3)}(\omega)$ will be strongly enhanced in the SPR region. It has been shown that there are three major electronic contributions to the Kerr nonlinearity in metal nanoparticles [Hache *et al.*]. The first one, $\chi^{(3)}_{intra}$, is derived from the intraband conduction electrons in the sp band. It is electric dipole in nature, originates totally due to the confinement of the free electrons, and is strongly size dependent. The second is from interband transitions between the d-bands and the conduction band which occurs when the photon energy is larger than a gap energy, $E_g = \hbar\omega_g$ (which is 1.7 eV for gold, corresponding to the X point of the first Brillouin zone). Interband transitions can saturate leading to a mostly imaginary and negative $\chi^{(3)}_{inter}$, and this contribution is size and shape independent down to very small sizes of about 2.5 nm. The third and most important contribution $\chi^{(3)}_{he}$ arises from hot electrons. By photoexcitation, conduction electrons can be easily elevated to temperatures of several hundred degrees as their specific heats are very small [Eesley, G. L.], [Schoenlein *et al.*] generating the hot electrons. It takes a few picoseconds for these electrons to thermalize with the lattice. During this time, the Fermi–Dirac electron distribution is modified, since part of the one-electron levels below the Fermi level is emptied and part of those above is occupied. This leads to a modification of the dielectric constant $\varepsilon(\omega)$, and the main contribution to the incremental $\delta\varepsilon_m$ will be from those states in the Brillouin zone for which the energy difference between the Fermi level and the d-bands is close enough to the excitation energy. For gold, at the photon energy of 2.33 eV, this comes from the L point of the Brillouin zone for which the gap is $\hbar\omega'_g \cong 2.4$ eV (the X point contributes only weakly to $\delta\varepsilon(\omega)$ since the corresponding gap of 1.7 eV is much smaller).Writing $\varepsilon(\omega) = \varepsilon_X + \varepsilon_L + \varepsilon_D$ where $\varepsilon_D$ is the Drude contribution of the free

electrons and $\varepsilon_X$ and $\varepsilon_L$ are components of $\varepsilon_{inter}$ with the suffixes denoting the X and L points of the Brillouin zone, respectively, we have $\delta\varepsilon(\omega) \cong (\partial\varepsilon_L/\partial T)\delta T$ where $\delta T$ is the change in temperature of the free electrons. This modification of $\varepsilon(\omega)$ results in a transient re-distribution of the equilibrium plasmon band: the absorption around the peak is reduced and that at the wings is increased. This reduction in absorption is generally referred to as 'plasmon band bleach' in literature [Logunov *et al.*], [Kamat *et al.*]. In the present case, we see this bleach in the form of humps flanking the valley in the z-scan curves, for input laser fluences in the range of 0.1 to 1 J/cm$^2$. Even in Ag where the plasmon peak is around 421 nm, we still see the bleach as far as at the excitation wavelength of 532 nm. As for the nonlinear susceptibility values, calculations show that the hot electron contribution $\chi^{(3)}_{he}$ to $\chi^{(3)}_{m}$ is mainly imaginary, and is larger in magnitude than $\chi^{(3)}_{intra}$ and $\chi^{(3)}_{inter}$. Four wave mixing experiments have shown that at 2.33 eV, values of $\chi^{(3)}_{he}$, $\chi^{(3)}_{inter}$ and $\chi^{(3)}_{intra}$ are in the order of $10^{-7}$, $10^{-8}$ and $10^{-10}$ esu respectively, for 10 nm diameter gold particles dispersed in silicate glass [Eesley, G. L.].

At higher laser fluences (from 1 to 10 J/cm$^2$) there is a shift to a substantially reduced transmission, which merits special attention because it renders practical applicability to the nanoparticles as optical limiters. Since this limiting is seen only at higher intensities and the excitation is by nanosecond pulses, a two-photon and/or two-step excitation of the system is highly likely, which can lead to such a transmission behaviour. In addition we also considered the possibility of nonlinear scattering here. Scattering is a fundamental display of light–matter interaction resulting from inhomogeneities in the refractive index, leading to a decrease of net transmission through the medium. Resonant excitation with nanosecond and longer pulses can result in thermally induced transient refractive index changes given by $\Delta n_0 = (dn_0/dt)F_0\alpha/2\rho C_v$, where $dn_0/dt$ is the thermo-optic coefficient, $\alpha$ the absorption coefficient, $F_0$ is the fluence, $\rho$ is the density and $C_v$ is specific heat at constant volume. Such nonlinear scattering contributes to optical limiting in a number of materials, including carbon black

[Tutt & Boggess], nanotube suspensions [Mishra *et al.*], and metal-dendrimer nanocomposites [Ispasoiu *et al.*]. From comparative studies in gold clusters of 5 and 30 nm average diameters, it has been previously suggested that the nanosecond limiting in these samples may be explained in the framework of nonlinear scattering [Francois *et al.*]. Previous studies in thiol-capped Ag, Au and Ag–Au alloy nanoparticles had revealed that for the same laser fluence, nanosecond limiting is more efficient than picosecond limiting [Philip *et al.,* 2001]. Therefore, to investigate the possibility of nonlinear scattering in the present samples, we did a few z-scans in which a photomultiplier tube (PMT) was used in addition to the existing detectors, to record the scattered radiation. The PMT was maintained at a radial distance of 5cm from the beam axis. By mounting the sample and PMT on the same translation stage, it was ensured that the PMT is maintained at the same distance (11cm) from the sample throughout the scan. The typical result obtained is shown in Fig. 2.6. It is seen that there is a substantial increase in scattering around the onset of limiting, and the point of maximum limiting coincides with that of maximum scattering. For further confirmation we took photographs of the transmitted beam using a CCD camera. When the sample was away from focus the beam preserved its shape, whereas when it was close to the focus ring-like patterns of scattered light could be seen around the central spot. These observations confirm the significant role of nonlinear scattering in the optical limiting behavior of our samples.

To estimate the strength of this nonlinearity, we numerically evaluate the quantity $\beta$ by fitting the z-scan curves (fig. 2.3) to the transmission equation (2.7) with $q_0$ replaced with $q\ (z) = \beta(1\text{-}R)\ I_0\ L_{eff} / [1 + (z/z_0)^2]$ where $I_0$ is the peak intensity at the focal point, and $z_0 = \pi\omega_0^2/\lambda$ is the Rayleigh range, where $\omega_0$ is the beam waist radius at focus and $\lambda$ is the light wavelength. This substitution is to get the transmittance at different z postions, z being the propagation axis along which the focused gaussian beam has an intensity gradient $I(z) = I(0) \Big/ \left[1 + \left(z/z_0\right)^2\right]$. $\beta$ in the present context represents nonlinearity that leads to a reduction in

transmission: it collectively represents two-photon absorption, reverse saturable absorption and nonlinear scattering. To do the fitting we chose only those z-scans obtained at a pump energy of 39 μJ in samples having a linear transmission of 0.48. The equation fits well in the valley region of the curves where limiting occurs, and in the wings where saturable absorption prevails the fit diverges from experimental points as expected. The β values have

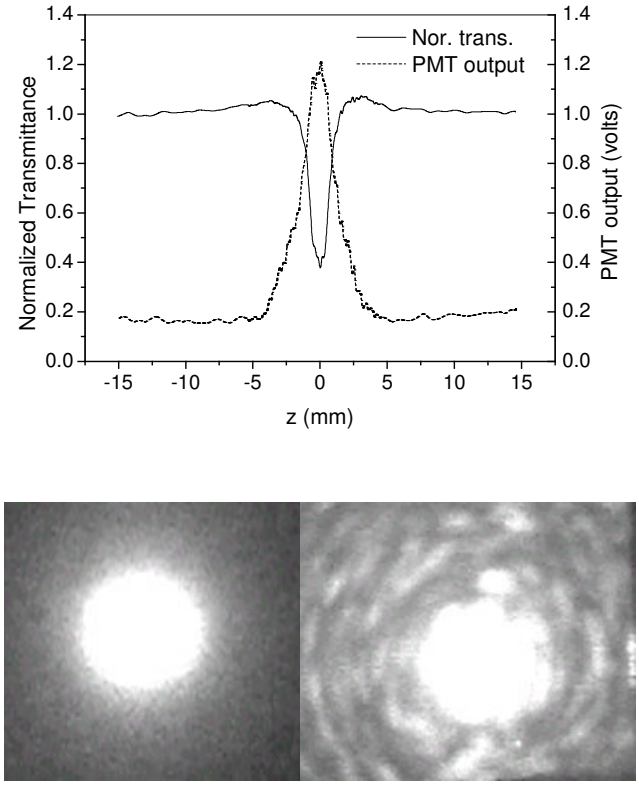


Figure 2.6: Nonlinear scattering in the metal nanoparticle suspensions. Solid line in the graph is the normalized transmittance for an Au@$SiO_2$ sample, while the dashed line is the corresponding scattering from the sample. The points of maximum limiting and maximum scattering coincide. Photographs show the transmitted beam when the sample is away from beam focus (left) and close to the focus (right).

been calculated to be in the order of $10^{-10}$ $mW^{-1}$ which indicates a substantial nonlinearity, and these values are comparable to those found for metal-chalcogenide clusters [Philip *et al*., 1999, 2000] and $C_{60}$ solutions [Couris *et al.*].

At this point, it would be informative to consider the photophysics of laser irradiation in these metal nanoparticles. Formation of photogenerated, strongly absorptive transient intermediate species has been reported in silver bromide nanoparticles in nanosols [Sahyun *et al.*] and suspended silver-containing nanoparticles [Sun *et al.*]. Kamat et al. have specifically assigned the strong, broadband transient absorption observed in colloidal silver particles of 40–60 nm diameter to a transient state generated by the photoejection of electrons from the parent cluster. They found that this charge separation leads to the break-up of clusters to form smaller particles (photofragmentation). However, since the plasmon band intensity increases with particle size in the size range of our interest, photofragmentation should lead to an increase in the linear transmission value. In fact, we found this to happen in just one of the various $Ag@ZrO_2$ samples we studied: before the experiment the linear transmission at 532nm was 0.58 and afterwards it was 0.77. On the other hand, $Ag@ZrO_2$ samples prepared in the other batches as well as the other samples studied did not show any change. Therefore, from the several measurements we carried out, we draw the conclusion that the samples we prepared do not normally undergo photofragmentation at the laser fluences used. This encourages us to investigate in more detail the exact mechanism of energy transport, i.e., how the free electrons communicate with the insulator shell, as there are no empty states to populate. Plasmon damping and electron–phonon scattering at the interface may be important, and more studies in particles of varying average sizes would be required to formulate a comprehensive understanding of the energy transport mechanism.

In short, our investigations show that oxide protected stable nanoparticles of Au and Ag exhibit either saturable absorption or optical limiting at 532 nm excitation, depending on the applied laser fluence. This behavior can be explained

in terms of the electronic Kerr nonlinearity and nonlinear scattering in the nanoparticles. The samples have been subjected to laser fluences up to 20 J $cm^{-2}$ and intensities up to 2.8 GW $cm^{-2}$, and no appreciable signs of laser-induced damage has been observed. The high laser damage threshold of oxide-protected metal nanoparticles is a promising step towards the realization of nanomaterial based optical limiters.

### 2.5 $Au_xAg_y@ZrO_2$ core–shell nanoparticles

From studies reported in the previous section we noted that oxide protection renders metal nanoparticles photosability under conditions of intense laser irradiation. For example, oxide-protected Au and Ag nanoparticles withstand laser fluences up to 20 J $cm^{-2}$ without damage. Moreover, protection by shells makes it possible to prepare materials in the form of thin films and disks. Therefore we investigated the optical nonlinearity of oxide protected Au:Ag alloy nanoparticles also, to study the effects caused by alloying. The particle size is approximately 30-40 nm in this case (fig. 2.7). The samples were synthesized by the group of Prof. T. Pradeep at the Indian Institute of Technology Madras, Chennai.

The *z*-scan curves obtained for $Au_{0.18}Ag_{0.82}@ZrO_2$, $Au_{0.3}Ag_{0.7}@ZrO_2$ and $Au_{0.46}Ag_{0.54}@ZrO_2$ suspended in 2- propanol are shown in Fig. 2.8A–C, respectively. Fig. 2.8D gives the normalized transmittance as a function of the input laser fluence. In general, an increase in transmission is seen at moderate laser fluences, and the net transmission decreases appreciably at higher fluences. However, the detailed features of the nonlinear transmission depend crucially on the alloy composition. As seen from the figure, the transmission increase is highest when the Au mole fraction is largest in the composite. Moreover, the effect is enhanced for higher sample concentrations within each composite. The optical limiting threshold (defined as the fluence at which the normalized transmittance drops to 0.5) is around 2.4 J $cm^{-2}$, except for $Au_{0.46}Ag_{0.54}@ZrO_2$, in

which the limiting threshold is much higher. In general the results obtained are similar to those obtained in the oxide-protected Au and Ag nanoparticles.

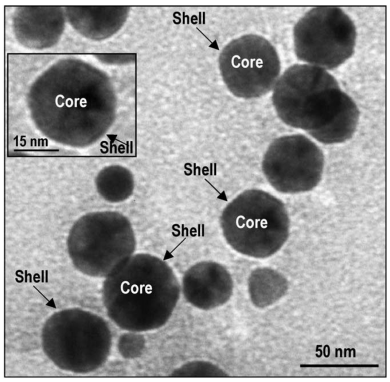


Figure 2.7: A transmission electron micrograph of the $Au_{0.46}Ag_{0.54}@ZrO_2$ core–shell nanoparticles taken by T. Pradeep's group. The core and the shell are clearly visible [from Nair, A.S. et al.].

As before, the plasmon band bleach is seen in the form of humps flanking the valley in the z-scan curves. The saturation is most prominent in $Au_{0.46}Ag_{0.54}@ZrO_2$, where the Au concentration is the largest. In fact, it is strong enough to push the sample's optical limiting threshold to more than 20 J $cm^{-2}$, as seen from Fig. 2.8D. This is a direct consequence of the red shift of the SPR with Au mole fraction, which brings it closer to the excitation wavelength of 532 nm. Therefore, the plasmon band bleach in the alloy system is dependent on its stoichiometry.

Fig. 2.9A shows the relative magnitudes of the bleach, obtained for various sample concentrations. At higher laser fluences the transmission is found to drop significantly, making the nanoparticles behave as optical limiters. To measure the contribution of nonlinear scattering, we monitored the output of the PMT that is located off-axis in our experiment, throughout the z-scans. The typical result obtained is shown in Fig. 2.9B. Comparing with Fig. 2.8, it is seen that the onset

of limiting is complementary to the increase in scattering, and the point of maximum limiting coincides with that of maximum scattering.

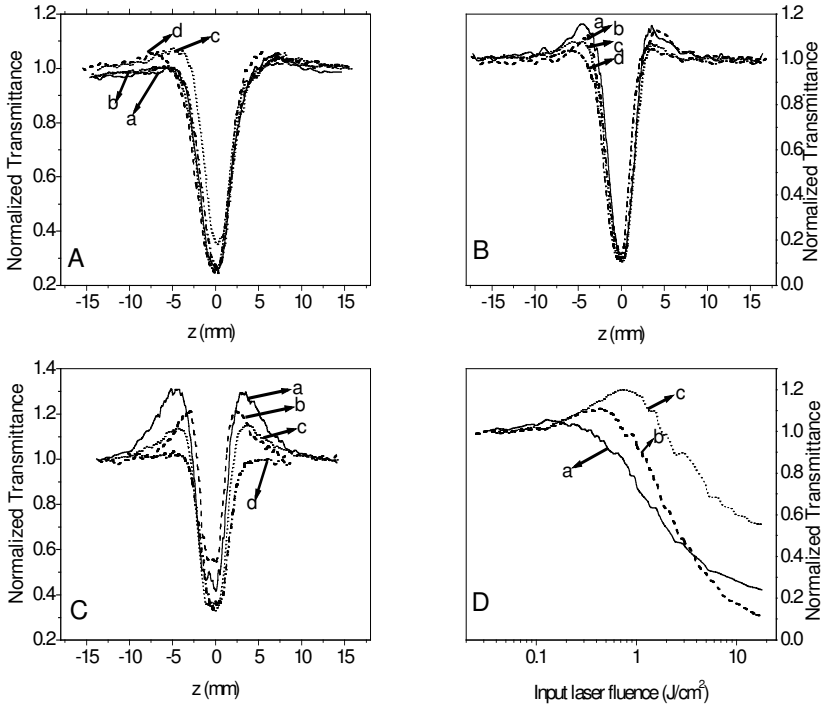


Figure 2.8: The *z*-scan curves obtained for the samples are shown in (A) ($Au_{0.18}Ag_{0.82}@ZrO_2$); (B) ($Au_{0.3}Ag_{0.7}@ZrO_2$); and (C) ($Au_{0.46}Ag_{0.54}@ZrO_2$). Laser pulse energy used is 30 μJ. Sample linear transmissions at 532 nm are: (a) 40%; (b) 50%; (c) 60%; and (d) 70%. The plasmon band bleach is most prominent in $Au_{0.46}Ag_{0.54}@ZrO_2$. (D) The normalized transmittance as a function of the incident laser fluence, for representative samples having a linear transmission of 50%: (a) $Au_{0.18}Ag_{0.82}@ZrO_2$; (b) $Au_{0.3}Ag_{0.7}@ZrO_2$; and (c) $Au_{0.46}Ag_{0.54}@ZrO_2$.

The scattering amplitude as a function of the sample concentration is given in Fig. 2.9C. A larger scattering is seen at lower concentrations. Interestingly, the net scattering is highest for $Au_{0.3}Ag_{0.7}@ZrO_2$, the cause of which is not well understood now. As shown in Fig. 2.9D, the β values are calculated to be in the order of $10^{-10}mW^{-1}$. For all the three alloys, the β values are found to peak around

a linear transmission of 0.5–0.6. Optical measurements reveal that significant nonlinear light scattering occurs in these core–shell alloys at high intensity laser irradiation, making these materials strong optical limiters with a high laser damage threshold.

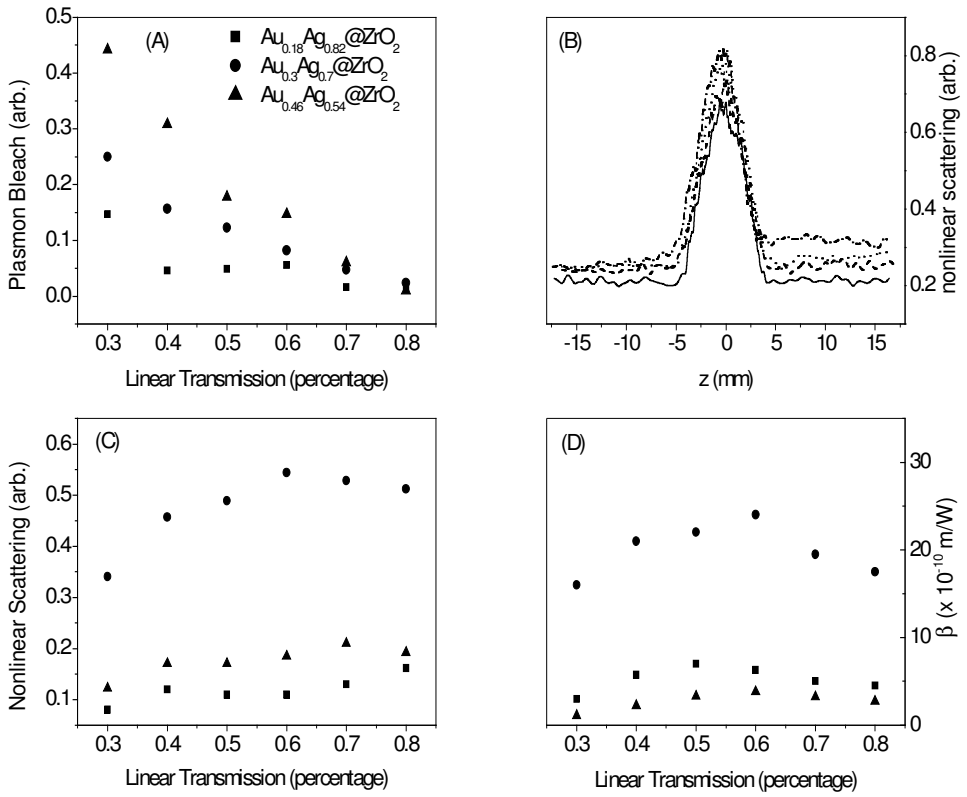


Figure 2.9: (A) Variation of the plasmon band bleach with sample concentration. (B) The PMT output, obtained for $Au_{0.3}Ag_{0.7}@ZrO_2$, showing large nonlinear scattering around the beam focus ($z$ = 0). Sample linear transmissions are: (a) 40%; (b) 50%; (c) 60%; and (d) 70%. (C) The relative magnitude of nonlinear scattering as a function of linear transmission. (D) Numerically calculated values of the nonlinearity coefficient $\beta$. The symbols correspond to the same composition as in (A).

## 2.6 Au:Ag nanocomposite polymer films

We also investigated the nonlinear optical properties of Au, Ag and AuAg nanocomposite polymer (NCP) films prepared in polyvinyl alcohol (PVA). The particle sizes are in the range of 5 to 15nm (fig 2.10). These samples were synthesized by Dr. B. Karthikeyan at the Raman Research Institute.

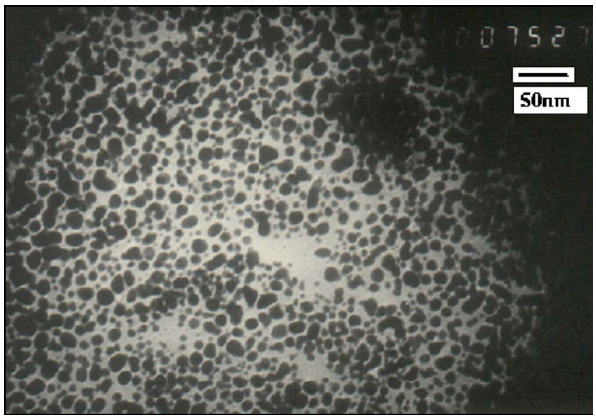


Figure 2.10: TEM image of the Ag-PVA film.

In addition to near-resonant excitation studies done at 532 nm, off-resonant studies also were done at 1064 nm, using 7 ns pulses in both cases. An absorption saturation behavior followed by an induced absorption was found for 532 nm excitation. At 1064 excitation, only an induced absorption is found, which is associated to an effective fifth order nonlinear process. These materials also have the potential to be used as saturable absorbers and optical limiters.

Figure 2.11 shows the nonlinear transmission observed at 532 nm. An absorption saturation behavior is found in films containing only Au. However, the saturation changes over to induced absorption in all other films when the input intensity is increased. This changeover in the sign of the nonlinearity is related to the interplay of plasmon band bleach and optical limiting mechanisms, as described in the previous sections. Since this behaviour repeatedly appears in the noble metal nanoparticles excited near the SPR, we decided to model the

nonlinear transmission in these materials accordingly. This can be done by defining a nonlinear absorption coefficient α(I) given by

$$\alpha(I) = \frac{\alpha_0}{1+(I/I_s)} + \beta I \qquad (2.15)$$

Where the first term on the RHS represents absorption saturation. $\alpha_0$ and $I_s$ are the linear absorption coefficient and saturation intensity respectively and β is an effective two-photon absorption coefficient.

The corresponding propagation equation is given as:

$$\frac{dI}{dz} = -\left(\frac{\alpha_0}{1+(I/I_s)} + \beta I\right) I \qquad (2.16)$$

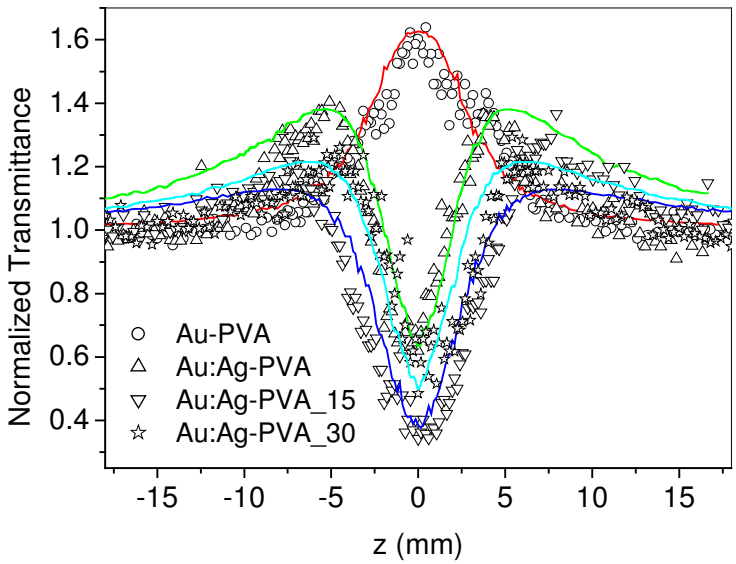


Figure 2.11: *Z*-scan curves of the samples obtained for 532 nm, 7 ns excitation. Solid lines are numerical fits to the experimental data. Laser pulse energy is 30 μJ.

By numerical fitting of the experimental data in fig. 2.11 to equation 2.16 we have calculated the $I_s$ and β values which are given in Table 2.1.

| Polymer nanocomposite film | $\beta(x10^{-9})$ (m/W) (excitation at 532nm) | Is $(x10^{11})$( $W/m^2$) (excitation at 532nm) | $\gamma(x10^{-24})(m^3/W^2)$ (excitation at 1064nm) |
|---|---|---|---|
| Au-PVA | 1 | 50 | 1.5 |
| Ag-PVA | 20 | 11 | 5 |
| Au:Ag-PVA | 70 | 8 | 200 |
| Au:Ag-PVA_15 | 159 | 6 | 200 |
| Au:Ag-PVA_30 | 70 | 8 | 240 |

Table 2.1: Values of the saturation intensity ($I_s$), two-photon absorption coefficient ($\beta$), and three-photon absorption coefficient ($\gamma$) calculated from numerical fits.

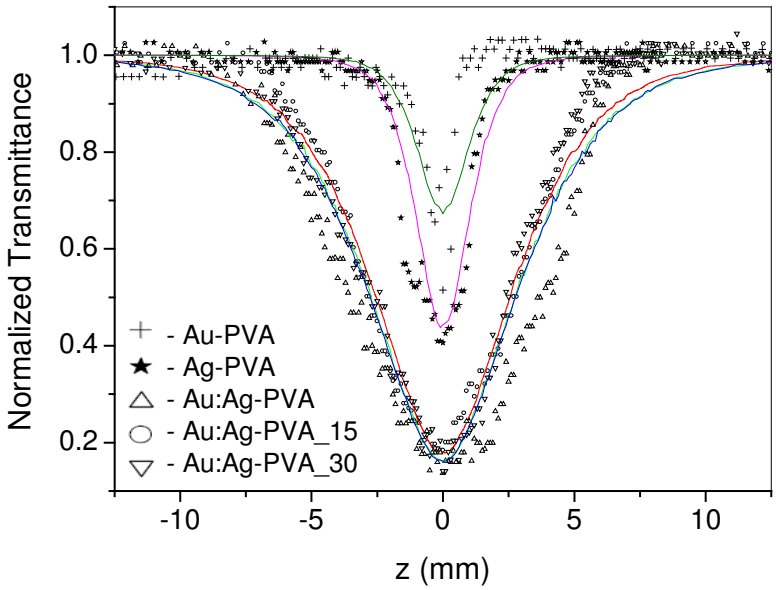


Figure 2.12: *Z*-scan curves of the samples excited at 1064 nm. Solid lines are numerical fits to the experimental data for a three-photon like absorption process. The laser pulse energy is 1 mJ.

Figure 2.12 shows the nonlinear absorption measured at 1064 nm. At this off-resonant excitation wavelength there is no local field enhancement within the

particles, and no one-photon resonant levels are present. Hence, higher pulse energies up to 1 mJ are required to induce nonlinearity in the films. Such high pulse intensities do not seem to cause any damage to the films. The experimental results are found to fit only for a three-photon like absorption behaviour, using equation 2.12. Interestingly, films containing only Au or Ag nanoparticles show a lower nonlinearity at this wavelength, while the alloy films clearly exhibit a higher nonlinearity. Even though the obtained nonlinearity fits only to a three-photon like absorption process it is unlikely that the underlying mechanism is pure three-photon absorption: in reality the process can be a sequential effect with a two-photon absorption ($\chi^{(3)}$ process) followed by an excited state single photon absorption ($\chi^{(1)}$ process), which effectively acts as a fifth ($\chi^{(5)}$) order process. Such phenomena have been reported in semiconductors before [Said *et al.*]. An effective three-photon absorption coefficient ($\gamma$) can be calculated from the numerical fits and the values obtained are given in table 2.1.

Thus for resonant excitation the sign of the nonlinearity is dependent on sample composition and input laser fluence in these samples, while for off-resonant excitation they exhibit only induced absorption. Hence the Au:Ag nanocomposite polymer films can be used either as saturable absorbers or optical limiters by choosing the appropriate excitation wavelength.

### 2.7 Small clusters of Au@alkanethiol

In the previous sections we found that an important deciding factor in the sign of the absorptive nonlinearity of metal nanoclusters is the surface plasmon resonance (SPR), which leads to saturable absorption-like behavior upon laser excitation. In fact SPR saturation could partially offset the limiting mechanisms in > 2 nm nanoclusters [Philip *et al.*]. Therefore in the present work, we have investigated the nonlinear transmission in smaller nanoclusters of Au@hexanethiol and Au@dodecanethiol, having particle sizes in the range of 1 nm. The SPR band is substantially suppressed in these clusters, so that the optical

absorption spectra show only a very weak structure around the SPR wavelength. Using 7 ns laser pulses at 532 nm, an exclusive optical limiting behavior has been observed, without any indications of an SPR bleach. The temporal dynamics of the nonlinearity also is studied using femtosecond pump-probe measurements at 400 nm. These samples were synthesized by Prof. T. Pradeep's group at the Indian Institute of Technology Madras, Chennai.

The cluster sizes were indirectly estimated from the mass spectrum of Au@hexanethiol, taken using a MALDI-TOF (Matrix Assisted Laser Desorption –Time of Flight) instrument. The mass of the cluster of interest was confirmed to be 29kDa showing that each cluster contains approximately 140 atoms of Au. Since the radius of a gold atom is approximately $175 \times 10^{-12}$ m, the radius of such a

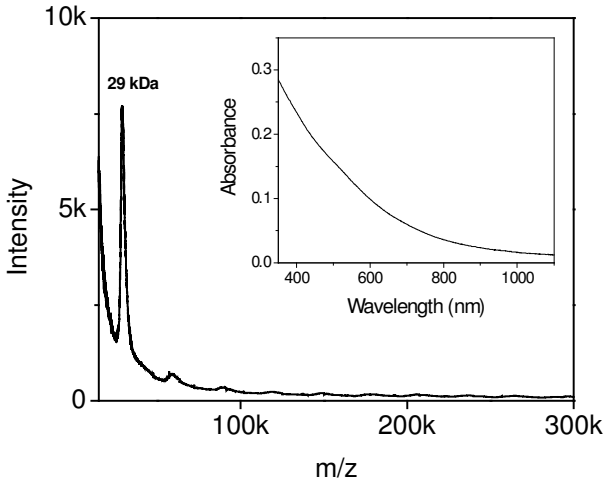


Figure2.13: MALDI-TOF spectrum of column separated Au@hexanethiol cluster compound with the matrix, indole acrylic acid (ratio 1:5) showing the presence of 29 kDa clusters exclusively. A minor peak due to the dimer formed during the ionization process is also seen. *Inset:* Optical absorbance spectrum of the same sample, showing an extremely weak surface plasmon resonance around 523 nm.

cluster will be in the order of 1 nm. When the near-absence of the SPR band in the UV/Vis spectrum (taken in a Perkin Elmer Lambda 25 UV/Vis spectrometer) also is considered, it can be concluded that the present sample contains 29 kDa cluster

compound exclusively. The MALDI and optical absorption spectrum are given in Fig.2.13. Similar MALDI and UV/VIS results have been obtained for Au@dodecanethiol clusters also.

From the z-scan curves (Fig.2.14), we find that the nonlinearity is essentially of the reduced transmission (optical limiting) type in these samples. Limiting shown by pure toluene is negligible here, and the limiting efficiency increases substantially with sample concentration. The nonlinear scattering amplitudes are nearly the same irrespective of the sample concentration, particularly at higher input fluences. Therefore the observed increase in limiting with sample concentration should have a non-thermal origin.

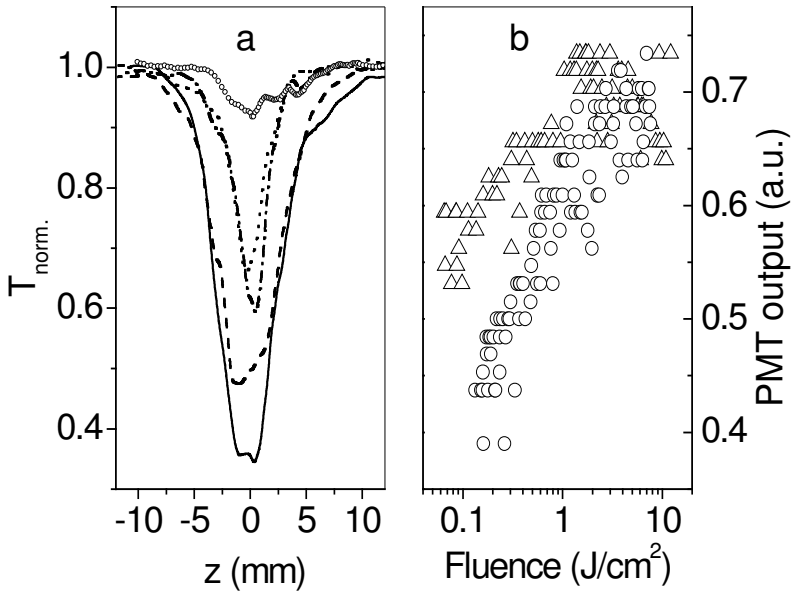


Figure 2.14: (a) z-scan curves obtained for the 29kDa Au clusters when excited with 532 nm, 7 ns pulses. The mean laser energy reaching the sample is 38 microjoules. Linear transmissions are: solid curve – 0.20, dash – 0.3, dash-dot – 0.47, and dot – 0.67. Circles represent pure toluene. (b) Induced scattering signals obtained from the PMT, as a function of the input laser fluence. Linear transmissions are: circles – 0.20, triangles – 0.67.

Figs.2.15A and 2.15B show the least squares fits obtained for a dilute, as well as a concentrated solution, respectively. Calculated SSEs (sum of squares error) show that in the dilute solution both the two-photon and three-photon equations fit with a similar accuracy, while the three-photon fit is much better in the concentrated solution. The numerically calculated value of the three-photon absorption coefficient is 2.9 x $10^{-21}$ $m^3W^{-2}$, for the concentrated sample. The real mechanism can be a sequence of one-photon absorptions ($\chi^{(1)}$: $\chi^{(1)}$: $\chi^{(1)}$), which effectively appears as a fifth order ($\chi^{(5)}$) process.

One way to test whether the nonlinearity is a direct $\chi^{(5)}$ effect or a sequential absorption effect is to study its dependence on laser pulsewidth. Results of our measurements are shown in Fig.2.16. When excited using 100 fs pulses (fluence: 1.04 J/$cm^2$, intensity: 1.04 x $10^{13}$ W/$cm^2$), pure toluene shows a strong limiting, which is not affected much by the addition of sample to it. On the other

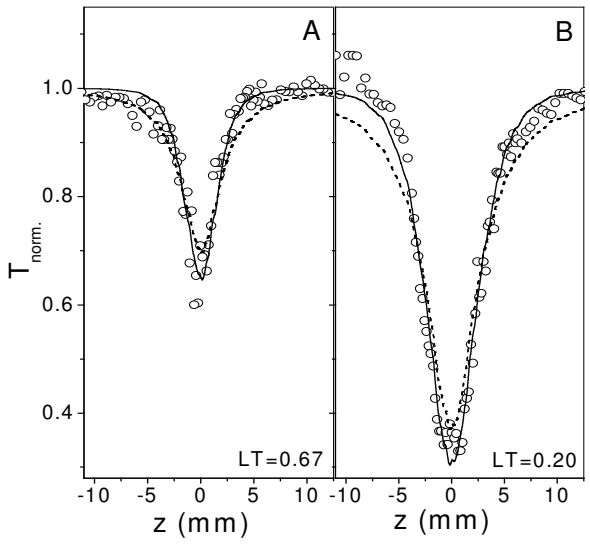


Figure 2.15: (A,B) Z-scan curves with numerical fits. Circles are data points. Solid curves are numerical fits to a three-photon absorption process while dotted curves are those for a two-photon absorption process. Linear transmissions are 0.67 and 0.20 as shown. The mean laser pulse energy is 38 microjoules.

hand, when excited with 7 ns pulses (fluence : 7.47 J/cm$^2$, intensity : 1.07 x 10$^9$ W/cm$^2$) toluene shows only a weak nonlinearity, which increases significantly on the addition of nanoclusters. Thus the nonlinearity in toluene is instantaneous and intensity-dependent, whereas that in the nanoclusters is accumulative. An accumulative nonlinearity indicates the involvement of a sequential nonlinear process.

Unlike in the case of semiconductors and metal colloids, the excitation dynamics in in these small clusters should be modeled in a molecular framework. This implies that the relative rigidity of the 140 atom cluster might impede the photogeneration of free carriers, but nevertheless, will not hinder the occurrence of an excited state absorption. At this point it is worthwhile to discuss the size-dependent transition of metal clusters from a "nanoparticle" to "molecular" type behavior. From studies in gold, [Link *et.al*.] have found strong evidence for the molecule-like behavior of a 28 atom gold core nanocluster surrounded by glutathione molecules. For instance, these clusters exhibit two separate luminescence bands with maxima at 1.5 and 1.15 eV (800 and 1100 nm respectively), and the luminescence lifetime is found to be in the order of nanoseconds to microseconds. Because of this unusually high life time, it was suggested that the short and long wavelength bands could be assigned to the fluorescence and phosphorescence from excited singlet and triplet states, respectively, in analogy to the photophysical properties of a molecule. Moreover, the excited state lifetimes were found to be independent of the pump intensity, revealing a single electron excitation dynamics typical of molecules. In comparison, in larger metal clusters (> 2-3 nm) which show the "nanoparticle" behavior, the prevalent plasmon excitation is a collective process, and the subsequent electron-phonon relaxation is strongly pump intensity dependent, due to the temperature dependence of the electronic heat capacity.

In the present case, however, the cluster contains about 140 atoms, and the SPR is extremely weak to the extent that no SPR bleach has been observed on

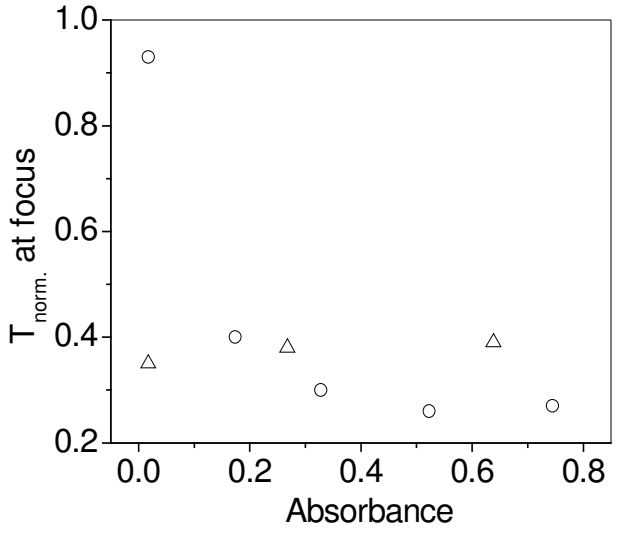


Figure 2.16: reduction in transmission as a function of laser pulsewidth and sample concentration. Normalized transmittance of the samples at the beam focus is plotted against sample absorbance (measurements are in a 1 mm cuvette). Absorbance of pure toluene is close to zero. Triangles - 100 fs pulses (400 nm), Circles - 7 ns pulses (532 nm).

laser excitation. Therefore the behavior is rather midway between that of a molecule and a nanoparticle, and hence, the term “semi-molecular” may be an appropriate description. It is therefore possible to consider a four-level system for the electron dynamics of the clusters, as shown in Fig. 2.17. For simplicity of calculation the electron excitation is reduced to a two-step process, where a two-photon induced excited state absorption is assumed. The linear transmission is normalized to unity in the calculations. In this scheme, two photons at 532 nm (2.33 eV) are required to reach the first nonlinearly excited state, from where a fast decay occurs to the LUMO (lowest unoccupied molecular orbital) level. A third photon is hence absorbed, in an excited state absorption process. It may be noted that in a nanoparticle model for Au clusters, two-photon absorption at 2.33 eV will correspond to the interband transitions from the d-band to the conduction band, and excited state absorption will correspond to free carrier absorption. The

LUMO state is relatively long-lived, and de-excitation occurs by radiative and non-radiative emissions bridging the HOMO (highest occupied molecular orbital) – LUMO gap. The corresponding set of rate equations can be written as:

$$\frac{dN_1}{dt} = -\frac{\sigma^{(2)}(N_1 - N_3)I^2}{2(h\nu)^2} + \frac{N_2}{\tau_2} \tag{2.17}$$

$$\frac{dN_2}{dt} = -\frac{\sigma^{(ex)}(N_2 - N_4)I}{h\nu} - \frac{N_2}{\tau_2} + \frac{N_3}{\tau_3} + \frac{N_4}{\tau_4} \tag{2.18}$$

$$\frac{dN_3}{dt} = \frac{\sigma^{(2)}(N_1 - N_3)I^2}{2(h\nu)^2} - \frac{N_3}{\tau_3} \tag{2.19}$$

$$\frac{dN_4}{dt} = \frac{\sigma^{(ex)}(N_2 - N_4)I}{h\nu} - \frac{N_4}{\tau_4} \tag{2.20}$$

and the propagation equation is,

$$\frac{dI}{dt} = \frac{-c}{n}\left\{\frac{\sigma^{(2)}(N_1 - N_3)I^2}{h\nu} + \sigma^{(ex)}(N_2 - N_4)I\right\} \tag{2.21}$$

where $N_n$ are the populations of the respective levels, I is the intensity of the laser pulse, $\sigma^{(2)}$ is the two-photon absorption cross section, and $\sigma^{(ex)}$ is the excited state absorption cross section. $\tau_n$ are the lifetimes of the respective levels.

These coupled rate equations are solved numerically by using the fourth order Runge-Kutta method. The system of equations (2.17 – 2.20) is solved for different input intensities and the corresponding output intensity is obtained by simultaneously solving the propagation equation 2.21. A smooth variation in the input intensity is obtained by calculating the intensity at each z position of the zscan experiment. The calculation procedure is as follows: Each slice of the temporal Gaussian pulse is passed through a slice of the sample in the cuvette along the laser propagation direction. The sample path length in the cuvette is 1mm. The population of each cuvette slice is modified by the passage of each slice of the input Gaussian pulse, and the transmitted intensity of that slice is in

turn affected by the population redistribution in that cuvette slice. The laser pulse slice with the transmitted intensity from the first cuvette slice is then propagated to the second cuvette slice, which contains the initially enrolled fresh population of the states. The rate equations are simultaneously solved. The population gets

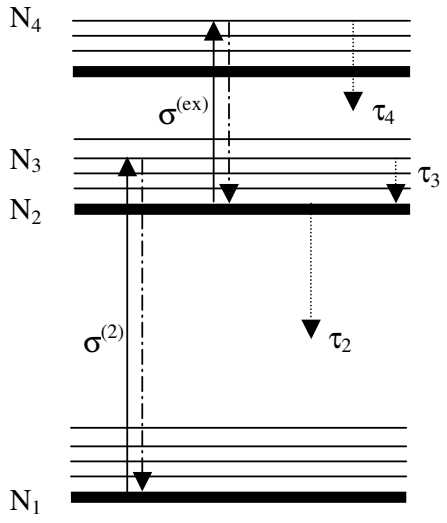


Figure 2.17: A schematic energy level diagram for the small Au clusters in the molecular approximation. Downward transitions drawn close to the absorption transitions represent stimulated emission. Other decays are represented by their respective lifetimes, $\tau_n$.

redistributed and the first laser pulse slice goes to the third cuvette slice and so on. Once the first laser pulse slice is out of the sample, all the cuvette slices have the redistributed population to which the second slice of the laser pulse is passed. The cycle repeats, which is done for all slices of the Gaussian pulse. The transmitted Gaussian pulse is then reconstructed from the output slices. The transmittance is obtained by dividing the output fluence by the input fluence.

Knowledge of $\tau_n$ is required to solve the above equations simultaneously for $\sigma^{(2)}$ and $\sigma^{(ex)}$ within reasonable limits of accuracy, and earlier studies have thrown some light into this aspect. For example, transient absorption studies in

$Au_{28}$ have revealed that when excited at 400 nm, and probed at longer wavelengths (> 500 nm), the excited state relaxation is a biexponential decay [Link *et al*]. A subpicosecond (about 750 fs) lifetime and another longer (> 1 ns) decay time are involved, independent of the laser pump power. The fast relaxation was attributed to the relaxation from the initially excited (Franck-Condon) state to the LUMO level. The longer decay time was assigned to the radiative and nonradiative recombinations taking place from the LUMO level, causing the final relaxation of the clusters. In our case the excited state relaxation time will be equal to the optical limiting lifetime of the nanoclusters.

To measure the excited state relaxation times of our samples, we did pump-probe studies using 100 fs, 400 nm pulses for pure toluene and the clusters. A weak fraction of the 400 nm pulse was used as the probe. Typical results are shown in Fig.2.18a. Interestingly, we observe only the fast component of the decay, and the slow component is absent. This is consistent with the observation in $Au_{28}$ that when the probe wavelength is decreased, the amplitude of the slow component also decreases, since the transient absorption peak is redshifted to 600 nm (2.07 eV) [Link *et al*].

From several pump-probe measurements we have estimated average values for the fast relaxation time, assuming a single exponential function. While pure toluene shows a lifetime of 501 ± 72 fs, hexanethiol protected clusters give a lifetime of 1.17 ± 0.15 ps, and dodecanethiol protected clusters give 1.63 ± 0.17 ps. This lifetime should correspond to $\tau_3$ in the energy level diagram. The radiative lifetime $\tau_2$ (which is not measured) should be in the order of nanoseconds in a molecular model [Link *et al.*], [Smith *et al.*] and lesser in a nanoparticle model. We solved the rate equation system numerically under both approximations, to obtain the corresponding values of $\sigma^{(2)}$ and $\sigma^{(ex)}$. Results are shown in Fig. 2.18b and 2.18c, and the values thus calculated are given in Table 2.2. These values are rather high, when compared to the typical absorption cross sections in organic molecules. It is therefore evident that the nonlinear absorption in the present

clusters is very strong. The optical limiting action is very fast (< 2ps) at the excitation wavelength of 400nm.

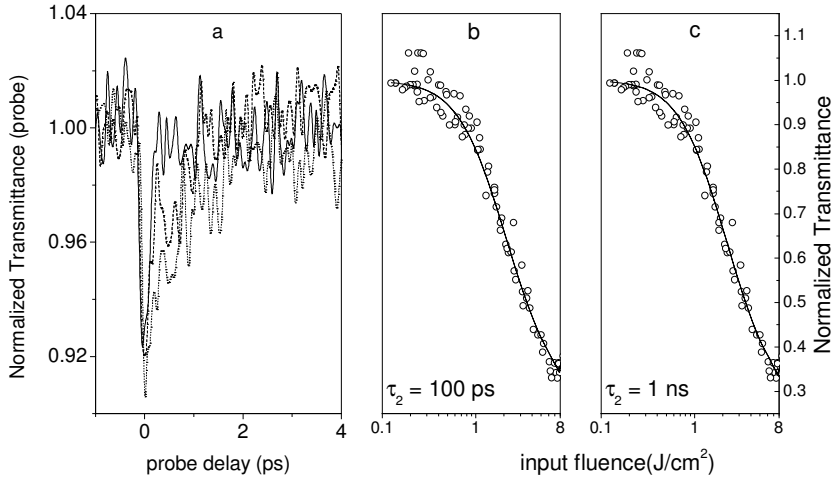


Figure 2.18: (a) Transmission recovery of the $Au_{140}$ clusters when excited and probed with 400 nm, 100 fs pulses. Solid curve – pure toluene, dashed curve – hexanethiol protected cluster, dotted curve – dodecanethiol protected cluster. (b,c) Normalized transmittance of the Au@hexanethiol clusters with input laser fluence. Sample linear transmission is 0.2. Solid curves are numerical fits obtained for two different values of $\tau_2$.

| Model | $\tau_2$ ps | $\tau_3$ ps | $\tau_4$ ps | $\sigma^{(2)}$ $cm^4s$ | $\sigma^{(ex)}$ $cm^2$ |
|---|---|---|---|---|---|
| Nanoparticle | 100 | 1.4 | 0.6 | 5.89E-45 | 9E-16 |
| Molecule | 1000 | 1.4 | 0.6 | 6.82E-46 | 9E-16 |

Table 2.2: Nonlinear absorption cross-sections calculated for Au@hexanethiol clusters under the nanoparticle and molecule approximations.

## 2.8 Conclusions

We investigated the absorptive optical nonlinearity of Au, Ag, and Au:Ag nanoparticles of different sizes in different host systems (liquids and thin films). Saturation of absorption and optical limiting are found, depending on particle size,

concentration and incident fluence. Therefore these materials can be used as fast saturable absorbers or optical limiters at appropriate concentrations, particle sizes and excitation wavelengths.